

PET Quantification of Tau Pathology in Human Brain with ^{11}C -PBB3

Yasuyuki Kimura*¹, Masanori Ichise*¹, Hiroshi Ito^{1,2}, Hitoshi Shimada¹, Yoko Ikoma¹, Chie Seki¹, Harumasa Takano¹, Soichiro Kitamura¹, Hitoshi Shinotoh¹, Kazunori Kawamura¹, Ming-Rong Zhang¹, Naruhiko Sahara¹, Tetsuya Suhara¹, and Makoto Higuchi¹

¹Molecular Imaging Center, National Institute of Radiological Sciences, Chiba, Japan; and ²Advanced Clinical Research Center, Fukushima Medical University, Fukushima, Japan

Tau accumulation in the brain is a pathologic hallmark of Alzheimer disease and other tauopathies. Quantitative visualization of tau pathology in humans can be a powerful method as a diagnostic aid and for monitoring potential therapeutic interventions. We established methods of PET quantification of tau pathology with ^{11}C -PBB3 (2-((1*E*,3*E*)-4-(6-(^{11}C -methylamino)pyridin-3-yl)buta-1,3-dienyl) benzo[*d*]thiazol-6-ol), considering its radiometabolite entering the brain. **Methods:** Seven Alzheimer disease patients and 7 healthy subjects underwent dynamic ^{11}C -PBB3 PET scanning. Arterial blood was sampled to obtain the parent and metabolite input functions. Quantification of ^{11}C -PBB3 binding was performed using dual-input models that take the brain metabolite activity into consideration, traditional single-input models without such considerations, and the reference tissue model (MRTM_O) and standardized uptake value ratio (SUVR). The cerebellar cortex was used as the reference tissue for all methods. **Results:** The dual-input graphical models estimated binding parameter (BP_{ND}^*) stably (~0.36 in high-binding regions). The MRTM_O BP_{ND}^* matched the corresponding BP_{ND}^* by the dual-input graphical model ($r^2 = 1.00$). SUVR minus 1 correlated well with MRTM_O BP_{ND}^* ($r^2 > 0.97$). However, BP_{ND} by the single-input models did not correlate with BP_{ND}^* by the dual-input graphical model ($r^2 = 0.04$). **Conclusion:** The dual-input graphical model BP_{ND}^* is consistent with the reference tissue BP_{ND}^* and SUVR-1, suggesting that these parameters can accurately quantify binding of ^{11}C -PBB3 despite the entry of its radiometabolites into the brain.

Key Words: PET quantification; tau; ^{11}C -PBB3; Alzheimer disease

J Nucl Med 2015; 56:1359–1365

DOI: 10.2967/jnumed.115.160127

Senile plaques and neurofibrillary tangles are the 2 pathologic hallmarks of Alzheimer disease (AD). Senile plaques consist of extracellular β -amyloid (A β) deposits (1,2). PET has been used

for detecting A β accumulations and also applied to monitor potential effects of A β immunotherapies (3–5). Neurofibrillary tangles consist of intraneuronal aggregates of hyperphosphorylated tau proteins (6). Since the tau pathology in AD is closely related to the neural death and cognitive dysfunction along with the amyloid pathology (7,8), it is a promising therapeutic target for AD (9,10). The tau pathology is also known in other neurodegenerative disorders such as progressive supranuclear palsy and corticobasal degeneration (11,12). Thus, a reliable quantitative visualization of tau accumulation would be essential for accurate diagnosis and the development of disease-modifying drugs targeting tau in diverse neurologic diseases (13,14).

Recently, we developed a new radioligand, ^{11}C -PBB3 (2-((1*E*,3*E*)-4-(6-(^{11}C -methylamino)pyridin-3-yl)buta-1,3-dienyl) benzo[*d*]thiazol-6-ol), for PET tau imaging (15). Our in vitro data indicated that ^{11}C -PBB3 binds reversibly to neurofibrillary tau tangles with high affinity ($K_{\text{D}} = 2.5$ nM) and selectivity (50-fold selectivity over A β deposits) (15). Of the other recently reported tau radioligands including THK families (16–19) and T80x (20,21), ^{11}C -PBB3 binds to tau lesions with a wide range of isoform compositions (15). The regional standardized uptake value ratio (SUVR) of ^{11}C -PBB3 in our previous ^{11}C -PBB3 PET studies reflected the known pathologic tau distribution at various stages of AD (22).

Our previous ^{11}C -PBB3 studies in humans and mice indicated that ^{11}C -PBB3 on intravenous administration is rapidly converted to a major radiometabolite in plasma, a significant amount of which has been shown to enter the mouse brain (23). This radiometabolite is expected to enter the human brain, which may complicate quantitative PET data analysis. It is therefore important to examine whether simplified quantitative measures such as SUVR accurately reflect specific binding of ^{11}C -PBB3 to pathologic tau deposits.

The purpose of the present study was to establish methods of quantifying ^{11}C -PBB3 binding considering the entrance of its radiometabolites into the human brain. We used dual-input models (24,25) that apply the unmetabolized parent and radiometabolite in the plasma as input functions. We found that the parameter SUVR minus 1 (SUVR-1) and the reference tissue model binding parameter (BP_{ND}^*) agreed with the dual-input model BP_{ND}^* , supporting the validity of these simplified models in quantifying tau pathology with ^{11}C -PBB3 PET.

MATERIALS AND METHODS

Participants

Seven AD patients and 7 elderly healthy controls (HCs) were enrolled (3 men/4 women for both groups; mean age \pm SD, 76 \pm 7 y for AD patients and 70 \pm 6 y for HCs). AD was diagnosed according

Received Apr. 30, 2015; revision accepted Jul. 9, 2015.

For correspondence or reprints contact either of the following:

Yasuyuki Kimura, Molecular Imaging Center, National Institute of Radiological Sciences, 4-9-1 Anagawa, Inage-ku, Chiba, Chiba 263-8555, Japan.

E-mail: y-kimura@nirs.go.jp

Masanori Ichise, Molecular Imaging Center, National Institute of Radiological Sciences, 4-9-1 Anagawa, Inage-ku, Chiba, Chiba 263-8555, Japan.

E-mail: ichisem@nirs.go.jp

*Contributed equally to this work.

Published online Jul. 16, 2015.

COPYRIGHT © 2015 by the Society of Nuclear Medicine and Molecular Imaging, Inc.

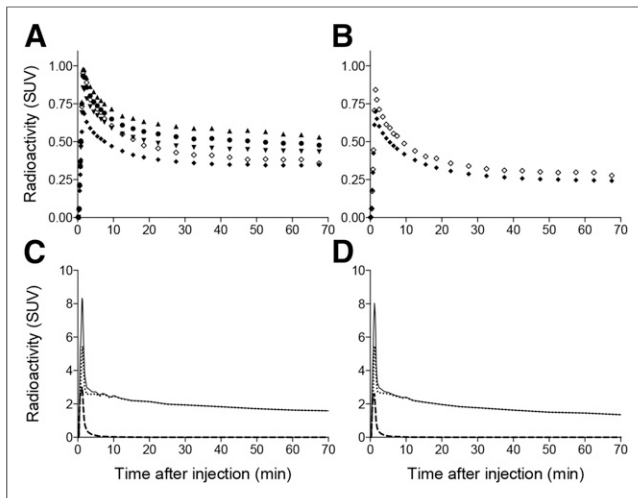


FIGURE 1. Time-activity curves in brain and arterial plasma after injection of ^{11}C -PBB3 in AD patients and HCs. Time-activity curves are shown for cerebral cortical regions with high (\blacktriangle), middle (\bullet), low (\blacktriangledown), and nonbinding (\blacklozenge) of ^{11}C -PBB3 and cerebellum (\diamond) in AD patients (A) and cerebral cortex (\blacklozenge) and cerebellum (\diamond) in HCs (B). Time-activity curves of total radioactivity (solid line), metabolite (dotted line), and parent (dashed line) in arterial plasma of AD patients (C) and HCs (D). Data represent mean of all 7 AD patients or 7 HCs.

to criteria of the National Institute of Neurologic and Communicative Diseases and Stroke/Alzheimer Disease and Related Disorders Association (26). The Clinical Dementia Rating scale (27) was 0.5 or 1 in AD patients and 0 in HCs. Mini-Mental State Examination scores (28) were 19.4 ± 2.4 in AD patients and 28.4 ± 2.2 in HCs. All HCs were free of major medical and neuropsychiatric illnesses. ^{11}C -labeled Pittsburgh compound B (3) PET scans were also obtained on the day of the ^{11}C -PBB3 PET studies, and all AD patients were positive and all HCs were negative for $\text{A}\beta$. This study was approved by the Radiation Drug Safety Committee and the Institutional Review Board of National Institute of Radiologic Sciences of Japan. Written informed consent or assent was obtained from all subjects. The study was registered with University Hospital Medical Information Network Clinical Trials Registry (UMIN000009052).

PET Imaging

^{11}C -PBB3 was produced as previously described (15,23). After an intravenous injection of ^{11}C -PBB3 (399 ± 45 MBq; specific activity, 88 ± 32 GBq/ μmol), 70-min dynamic PET scans were conducted using an ECAT Exact HR+ system (Siemens AG). PET images were reconstructed with a filtered backprojection method with corrections for attenuation and scatter. The dynamic scan consisted of 6×10 s, 3×20 s, 6×1 min, 4×3 min, and 10×5 min frames.

Measurement of ^{11}C -PBB3 in Plasma

Manual arterial blood samples were concurrently obtained 30 times with PET. Each blood sample was centrifuged, and the radioactivity concentrations in whole blood and plasma were measured. The plasma fractions of the parent and its radiometabolites were determined by high-performance liquid chromatography from 6 samples. Acetonitrile was added to each plasma sample, and the samples were then centrifuged and subjected to radio-high-performance liquid chromatography ($\mu\text{Bondapak C18}$ column [Waters], 7.8×300 mm; acetonitrile/ammonium formate mobile phase with gradient elutions = 40/60, 52/48, 80/20, 80/20, 40/60, and 40/60 at 0, 6, 7, 8, 9, and 15 min, respectively; flow rate, 6 mL/min). Two-exponential functions were used to interpolate the fraction of the parent and radiometabolites to obtain input functions.

Quantification Models

To quantify ^{11}C -PBB3 specific binding to tau, we used dual-input models that use both parent and metabolite input functions, single-input models that use a parent-only input function, and the reference tissue model and SUVR-1 that do not require blood data.

Dual-Input Models. We estimated ^{11}C -PBB3 binding parameters BP_{ND}^* and BP_{P} (namely specific distribution volume [V_{S}] (29)) in 2 ways using dual-input graphical analyses developed by Ichise et al. (24,30). This graphical model is derived from the dual-input compartment model (24,25). This graphical model has the following 2 operational equations, both of which allow estimation of BP_{ND}^* and BP_{P} when the system reaches transient equilibrium between the brain and plasma compartments (t^*).

$$\frac{\int_0^t C_b(t) dt}{C_b(t)} = \alpha(t) \frac{\int_0^t C_a^{\text{P}+\text{M}}(t) dt}{C_b(t)} + \beta(t), \quad \text{Eq. 1}$$

$$\frac{\int_0^t C_b(t) dt}{C_b(t)} = \alpha^{\text{P}} \frac{\int_0^t C_a^{\text{P}}(t) dt}{C_b(t)} + \alpha^{\text{M}} \frac{\int_0^t C_a^{\text{M}}(t) dt}{C_b(t)} + \beta(t), \quad \text{Eq. 2}$$

where C_a^{P} , C_a^{M} , and C_b are the radioactivity concentrations of the plasma parent, radiometabolite, and brain, respectively. $C_a^{\text{P}+\text{M}} = C_a^{\text{P}} + C_a^{\text{M}}$. In Equation 1,

$$\alpha = [1/(1 + \delta)]\alpha^{\text{P}} + [\delta/(1 + \delta)]\alpha^{\text{M}}, \quad \text{Eq. 3}$$

where δ is the plasma metabolite/parent concentration ratio at equilibrium (Supplemental Appendix A; supplemental materials are available at <http://jnm.snmjournals.org>) (24). In Equations 2 and 3, α^{P} and α^{M} represent the total distribution volumes of the parent (V_{T}^{P}) and radiometabolite (V_{T}^{M}), respectively. Assuming that the nondisplaceable distribution volume of the parent (V_{ND}^{P}) or the radiometabolite (V_{ND}^{M}) is the same in the target and reference tissues, BP_{ND}^* and plasma binding potential (BP_{P}) are calculated from the α 's of tau-rich target and tau-free reference tissues as

$$BP_{\text{ND}}^* = \frac{V_{\text{S}}}{V_{\text{ND}}^{\text{P}} + \delta V_{\text{ND}}^{\text{M}}} = \frac{\alpha_{\text{target}}}{\alpha_{\text{reference}}} - 1. \quad \text{Eq. 4}$$

$$BP_{\text{P}} = V_{\text{S}} = (1 + \delta)(\alpha_{\text{target}} - \alpha_{\text{reference}}). \quad \text{Eq. 5}$$

From Equation 2, BP_{ND}^* can also be calculated as follows:

$$BP_{\text{ND}}^* = \frac{\alpha_{\text{target}}^{\text{P}} - \alpha_{\text{reference}}^{\text{P}}}{\alpha_{\text{reference}}^{\text{P}} + \delta \alpha_{\text{reference}}^{\text{M}}} \quad \text{Eq. 6}$$

Here, we defined the parameter expressed by Equation 4 as BP_{ND}^* with an asterisk to distinguish it from the original definition of BP_{ND} (29), because BP_{ND}^* includes an additional metabolite distribution volume term, $\delta V_{\text{ND}}^{\text{M}}$, in the denominator. We considered BP_{ND}^* as an extension of the definition of BP_{ND} because this BP_{ND}^* is also directly proportional to $B_{\text{avail}}/K_{\text{D}}$, where B_{avail} is the target concentration (Appendix).

Single-Input Models. For the graphical analysis with unmetabolized ^{11}C -PBB3 as an input function, Logan plots were applied (31). For the compartment model analysis, the standard 2-tissue-compartment (2TC) model was applied (32). BP_{ND} and BP_{P} values were calculated from total distribution volumes in the target and reference tissues.

Reference Tissue Model. Reference tissue BP_{ND}^* estimated without blood data is the (tissue ratio-1) at equilibrium and is theoretically

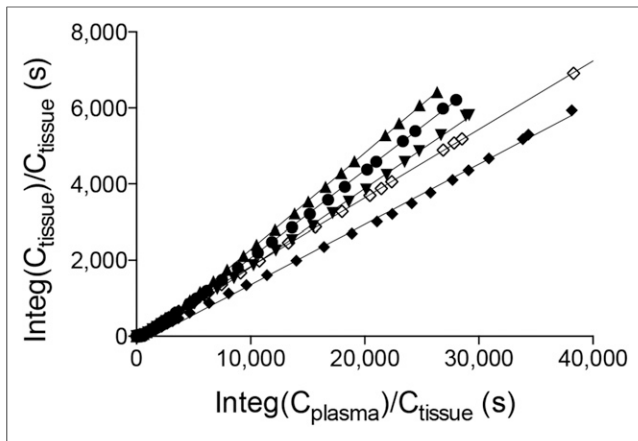


FIGURE 2. Dual-input graphical plots with plasma-input function (Eq. 1) in representative AD patients. Plots became linear after $t^* = 11$ min for cerebral cortical regions with high (\blacktriangle), middle (\bullet), low (\blacktriangledown), and non-tau-binding (\blacklozenge) regions and cerebellum (\diamond).

equivalent to dual-input BP_{ND}^* given by $\frac{V_s}{V_{ND}^* + \delta V_{ND}^*}$, if the metabolite enters the brain (24). We used the original multilinear reference tissue model (MRTM_O) to estimate BP_{ND}^* using region-of-interest (ROI) data and also to generate voxelwise parametric images of BP_{ND}^* using the cerebellar cortex as reference tissue (33). To evaluate the effect of shortening the scan length, BP_{ND}^* values from parametric images with truncated scan data (30, 40, 50, and 60 min) were calculated and compared with the BP_{ND}^* values from the full 70-min scan length.

SUVR. We obtained SUVR-1 ROI values from the summed PET images for 20–30, 30–50, and 50–70 min normalized to the cerebellar cortex.

PET Data Preparation

In our preliminary ¹¹C-PBB3 data analysis, the 2TC model with arterial data for small ROIs was unstable due to rapidly clearing parent input functions and overall low brain ¹¹C-PBB3 uptake. To improve the statistical quality of PET ROI data, we defined ROIs as follows (Supplemental Fig. 1): individual cerebral cortical masks were first created on segmented T1-weighted MR images using statistical parametric mapping (SPM12; Wellcome Trust Centre for Neuroimaging, U.K.). Then, for AD patients, we generated 3–4 cerebral cortical ROIs pooling all voxels of high (>0.3, high), medium (0.15–0.3, middle), low (0–0.15,

low), and nonbinding (<0) BP_{ND}^* values on preliminarily generated MRTM_O parametric images by applying coregistered cerebral cortical masks. These 4 sets of ROIs had a sample volume of 12 ± 6 , 50 ± 27 , 103 ± 35 , and 188 ± 64 cm, respectively. For HCs, we created 1 large entire cortical ROI (440 ± 34 cm), because cerebral cortical BP_{ND}^* was uniformly low. We used the cerebellar cortex as the reference tissue because there was negligible tau pathology in the postmortem AD cerebellum (34). Cerebellar cortical ROIs were manually defined on the coregistered T1-weighted MR images (7.8 ± 1.9 cm). All ROIs were further modified on the PET images to avoid high radioactivity spilling in from the adjacent venous sinuses. ROI time–activity curves were generated from the coregistered dynamic PET data. All image data analyses were performed in PMOD 3.6 (PMOD Technologies Ltd.).

Comparison Analysis

We compared BP_{ND}^* and SUVR-1 values among the different models, the main purpose of which was to examine how closely reference tissue BP_{ND}^* and SUVR-1 that use no blood data match corresponding BP_{ND}^* by dual-input models that use both plasma parent and metabolite data or single-input models BP_{ND}^* that use only plasma parent data. These comparisons were performed by calculating Pearson correlation coefficients (r^2).

RESULTS

Time–Activity Curves

The brain ¹¹C-PBB3 time–activity curves quickly peaked within a few minutes of intravenous injection of ¹¹C-PBB3 (1 SUV in AD and 0.8 SUV in HC) (Figs. 1A and 1B), and then washed out quickly initially and then slowly. Plasma parent time–activity curves peaked quickly and decreased also quickly thereafter (Figs. 1C and 1D). One major radiometabolite of ¹¹C-PBB3 appeared quickly in the plasma and slowly decreased thereafter, accounting for 90% of the total plasma radioactivity at 3 min (Supplemental Figs. 2A and 2B).

¹¹C-PBB3 Binding Parameter Estimation

Dual-Input Models. Graphical plots (Eq. 1) with a combined (parent + radiometabolite) plasma input became linear early after the radioligand injection (Fig. 2) when both α and β could be considered constant (24). α estimations were stable within 5%, with t^* varying from 11 to 40 min, and we fixed the t^* value to 11 min for all subjects. There was no significant difference in δ estimates between AD patients (78 ± 22) and HCs (88 ± 28)

TABLE 1
Binding Potential Values Estimated by Dual-Input Models, Single-Input 2TC Model, MRTM_O, and SUVR-1 Values

ROIs	Dual-input (Eqs. 1 and 5) BP_P	Dual-input (Eq. 1) BP_{ND}^*	Dual-input (Eq. 2) BP_{ND}^*	2TC BP_{ND}^{\dagger}	MRTM _O BP_{ND}^*	SUVR-1
AD patients						
High binding	5.94 ± 1.03	0.36 ± 0.07	0.44 ± 0.14	1.06 ± 0.66	0.37 ± 0.08	0.42 ± 0.09
Middle binding	4.24 ± 0.52	0.25 ± 0.02	0.28 ± 0.05	1.10 ± 0.67	0.26 ± 0.03	0.30 ± 0.04
Low binding	1.94 ± 0.32	0.12 ± 0.03	0.11 ± 0.03	2.09 ± 0.90	0.12 ± 0.03	0.16 ± 0.04
Nonbinding	-2.12 ± 0.69	-0.12 ± 0.02	-0.15 ± 0.03	5.03 ± 0.00	-0.13 ± 0.03	-0.08 ± 0.04
Normal control						
Cerebral cortex	-2.23 ± 0.80	-0.14 ± 0.07	-0.13 ± 0.08	0.10 ± 0.66	-0.15 ± 0.07	-0.15 ± 0.08

[†] BP_{ND} values from limited number of regions in which values were able to be estimated by 2TC model.

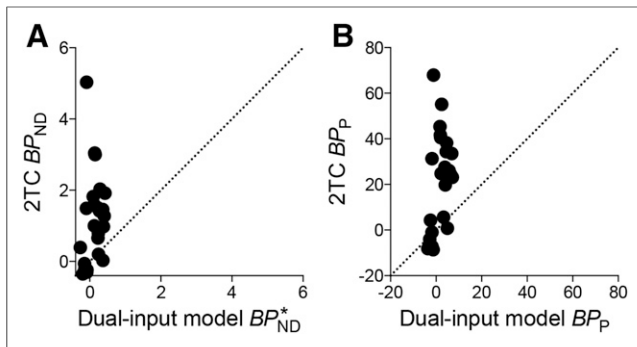


FIGURE 3. Correlation of binding potential values estimated by dual-input graphical model with combined plasma-input and single-input compartment model (2TC). Neither 2TC BP_{ND} (A) nor BP_P (B) correlated well with dual-input graphical BP_{ND}^* or BP_P ($r^2 = 0.04$ or 0.13), respectively. Straight line indicates line of identity in this and subsequent figures as applicable.

($P = 0.5$). The estimated BP_{ND}^* and BP_P values (Eqs. 4 and 5) in the high- and middle-binding regions were up to 3 and 2 times higher, respectively, than the parameter values in the low-binding regions, and these 2 sets of parameter values were highly correlated ($r^2 = 0.97$) (Table 1; Supplemental Fig. 3A). Both BP_{ND}^* and BP_P values were negative in the nonbinding regions of AD and HC. The 2 sets of BP_{ND}^* values from Equations 1 (combined plasma input) and 2 (separate parent and metabolite input) closely matched with each other ($r^2 = 0.97$, Supplemental Fig. 4; Table 1).

Single-Input Models. The graphical analysis with the parent-only input did not allow stable estimation of total distribution volumes, because the graphical plots were not linear within the PET scanning time (i.e., t^* could not be identified). The standard 2TC model with plasma parent as an input function was unstable in estimating total distribution volume in some cerebral cortical regions. The BP_{ND} values were estimated in the rest of the regions but with large parameter estimation variations ranging from 0.03 to 5.03 and from -0.35 to 1.49 in the cerebral cortex of AD patients and HCs, respectively. The 2TC BP_{ND} did not correlate well with the dual-input graphical BP_{ND}^* ($r^2 = 0.04$, Fig. 3A). The 2TC BP_P values also showed large parameter estimation variations ranging from 0.8 to 68 and from -8.6 to 31 in AD patients and HCs, respectively. Likewise, the 2TC BP_P did not correlate well with the dual-input graphical BP_P ($r^2 = 0.13$, Fig. 3B).

SUVR and Reference Tissue Model. The 3-dimensional plots of $MRTM_O$ were linear after t^* (Supplemental Fig. 5). $MRTM_O$ robustly estimated BP_{ND}^* for the ROI data and enabled stable voxelwise parametric imaging of BP_{ND}^* . The BP_{ND}^* estimated by the ROI-based $MRTM_O$ analysis closely matched plasma-input BP_{ND}^* and correlated highly with BP_P by the dual-input graphical model with a combined plasma input ($r^2 = 1.00$ and 0.96 ; Fig. 4 and Supplemental Fig. 3B, respectively). The BP_{ND}^* values in the ROIs placed on the parametric images slightly underestimated the corresponding BP_{ND}^* values in the ROI analysis (by 4%, $r^2 = 0.99$, Supplemental Fig. 6). The $MRTM_O$ parametric images showed a clear contrast of BP_{ND}^* values in the cerebral cortices including the hippocampal formation between AD and HC (Figs. 5A and 5B). Because ^{11}C -PBB3 accumulates prominently in the extra-brain venous sinus system, these regions also showed high false BP_{ND}^* values in both AD and HC. The SUVR-1 images with 30- to

50-min data also showed a clear contrast between AD and HC (Figs. 5C and 5D).

$MRTM_O$ parametric images of shortened-scan length showed underestimation of BP_{ND}^* values compared with the parametric images with 70-min scan data. The amount of underestimation of BP_{ND}^* values was 5%–10% for 60-min scan data (Fig. 6A). SUVR-1 values correlated well with parametric BP_{ND}^* values ($r^2 > 0.97$). However, SUVR-1 values with 30- to 50-min and 50- to 70-min data overestimated whereas 20- to 30-min data underestimated (5%–12%) those with full 70-min data or $MRTM_O$ BP_{ND}^* values (Fig. 6B).

DISCUSSION

We established methods for quantification of tau pathology in the human brain using ^{11}C -PBB3. The dual-input graphical models with an assumption of radiometabolites entering brain accurately estimated specific binding parameter BP_{ND}^* , which was consistent with the $MRTM_O$ BP_{ND}^* and SUVR-1 but not consistent with the traditional 2TC BP_{ND} . Reference tissue model BP_{ND}^* and SUVR-1 thus accurately quantified radioligand binding to tau despite the radiometabolite presence in the brain.

Significant amounts of the major radiometabolite of ^{11}C -PBB3 were found to enter the mouse brain (30% of radioactivity in the brain 5 min after injection) (23). In the human blood, ^{11}C -PBB3 was also rapidly metabolized, and a major radiometabolite identical to that observed in mice was produced, and this metabolite is very likely to enter the brain, although it is more hydrophilic than ^{11}C -PBB3. We recently identified the chemical structure of this radiometabolite, and we are trying to synthesize it to measure its binding affinity for tau (H. Hashimoto et al., unpublished data, 2015). We assumed in our data analysis that this radiometabolite has no significant affinity for tau. However, if the backbone structure of ^{11}C -PBB3 as a β -sheet ligand is preserved in the metabolic

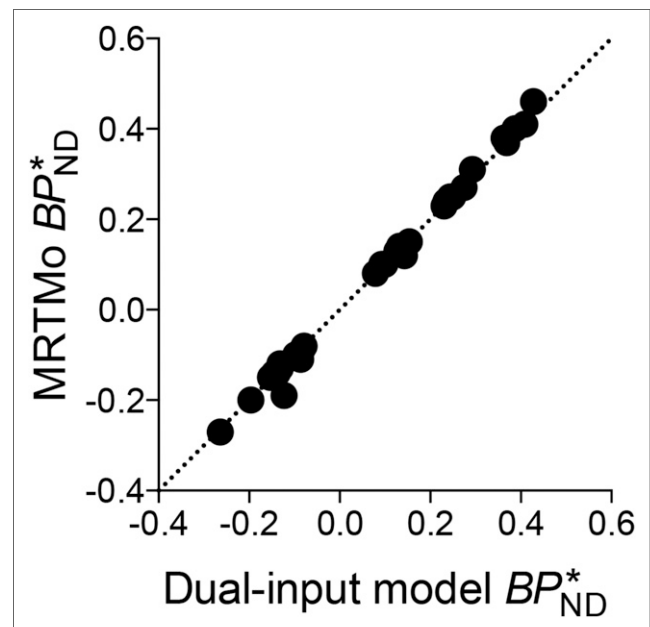


FIGURE 4. Correlation of BP_{ND}^* values estimated by dual-input graphical model with combined plasma-input and reference tissue model. BP_{ND}^* estimated by ROI-based $MRTM_O$ analysis closely matched BP_{ND}^* by dual-input graphical model ($r^2 = 1.00$).

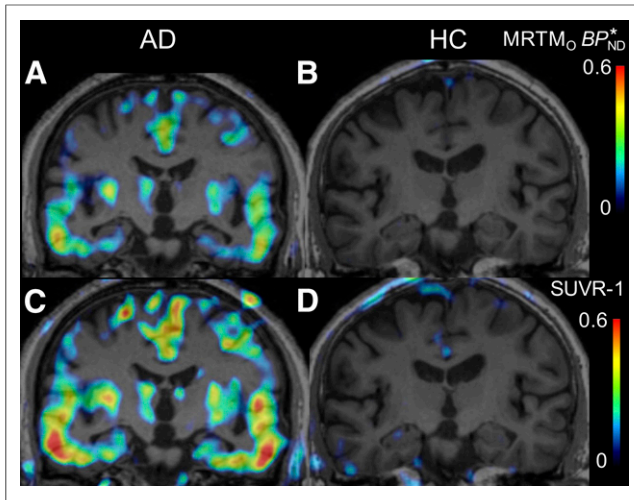


FIGURE 5. Coronal parametric images of AD and HC. MRTM_O was used to estimate parametric BP_{ND}^* value images in AD patients (A) and HCs (B). SUVR-1 images were created by averaging frames of PET images for 30–50 min in AD patients (C) and HCs (D).

conversion, it may also bind to tau. Nevertheless, current BP_{ND}^* by dual-input graphical analysis and MRTM_O can be also shown to be directly proportional to B_{avail} (Supplemental Appendix B).

In the present study, the dual-input graphical analysis with a combined plasma input allowed robust estimation of BP_{ND}^* . Although only Equation 1 is needed to estimate BP_{ND}^* , Equation 2 also allows calculation of the same BP_{ND}^* by estimating V_{ND}^M and V_T^P separately, although it requires δ (Supplemental Appendix A). We also applied dual-input compartment analysis (24,25). However, unlike the situation previously reported for ¹²³I-epidepride (24,25), this analysis for ¹¹C-PBB3 was unstable. The reason for this is that the model estimates 6 microparameters with a rapidly decreasing parent input as 1 of the 2 inputs as opposed to the graphical analysis estimating only macroparameters (V 's). However, we were able to show that, by providing the values estimated by the graphical analysis, the dual-input compartment model fairly well described measured time–activity curve data (Supplemental Figs. 7A and 7B). We applied the Logan plot to the predicted target brain time–activity curve due to the parent and found the plot was linear after $t^* = 11$ min (Supplemental Fig. 7C), indicating that parent components of time–activity curves reach transient equilibrium and ¹¹C-PBB3 binding is reversible.

Meanwhile, the conventional 4-parameter 2TC model with a parent input alone, assuming no metabolites entering the brain, was also unstable in estimating microparameters. With V_{ND} constrained to that of the cerebellar cortex, the macroparameter, BP_{ND} , could be estimated albeit with a large estimation variability. However, these BP_{ND} values did not match the BP_{ND}^* values estimated by the dual-input models and MRTM_O or SUVR-1 values. A model relying solely on unmetabolized ¹¹C-PBB3 as an input function may technically yield a valid binding parameter, BP_P (25), only if the brain time–activity curves can be reliably fitted with the parent-only input. This may not be feasible when significant metabolite activity is present in the brain as in the present study.

MRTM_O BP_{ND}^* estimation does not require any assumption of metabolite, because the estimation is performed without blood data. The validity of this estimation was supported by the agreement of BP_{ND}^* values between MRTM_O and the dual-input models.

The same MRTM_O operational equation can be derived from both the graphical analysis with parent-only input and the dual-input graphical analysis with combined plasma input (Eq. 1). In the present study, MRTM_O BP_{ND}^* values as expected closely matched those with the dual-input model but not with the single-input model. In addition, the SUVR-1 at 30–50 min showed excellent correlations with MRTM_O BP_{ND}^* and hence dual-input model BP_{ND}^* . Thus, the MRTM_O BP_{ND}^* and SUVR-1 appear to reflect tau binding even in the presence of radiometabolite in the brain. Finally, voxelwise BP_{ND}^* estimation by MRTM_O was stable, and the generated parametric images allowed clear delineation of tau deposition in the brain of AD patients in contrast to the absence of brain areas with positive BP_{ND}^* in HCs. Unlike most A β imaging radioligands, ¹¹C-PBB3 showed no overt retention in the white matter.

In the cerebral cortex of HCs and nonbinding regions of AD patients, BP_{ND}^* was slightly negative. This result is attributable to the fact that the nondisplaceable distribution volumes in the cerebellar cortex ($V_{ND}^P + \delta V_{ND}^M$) of both HCs and AD patients (16.7 ± 4.7 in HCs and 16.9 ± 2.6 in AD patients with no differences between the 2 groups) were slightly larger than those in the cerebral cortex of HCs (14.8 ± 5.0) and nonbinding regions of AD patients (14.3 ± 2.0). The exact reason for these regional differences in the nonspecific binding of ¹¹C-PBB3 is unclear at present. However, higher nonspecific binding or the presence of specific binding in the reference tissue theoretically does not violate the use of the reference tissue models when fitting is adequate (35).

The variability of BP_{ND}^* estimations by MRTM_O is known to be small compared with other reference tissue models (33). However, MRTM_O may underestimate BP_{ND} in the presence of noise in PET data, and this underestimation is more marked with larger noise and larger BP_{ND} values (33). Our parametric MRTM_O BP_{ND}^* was not significantly underestimated, compared with BP_{ND}^* determined by ROI-based MRTM_O (Supplemental Fig. 6), suggesting that the underestimation due to data noise is minimal, because the BP_{ND}^* for ¹¹C-PBB3 is small ($BP_{ND}^* < 0.5$).

BP_{ND}^* by definition includes δ (a constant value). There may be intersubject variations and potential drug treatment effects on the

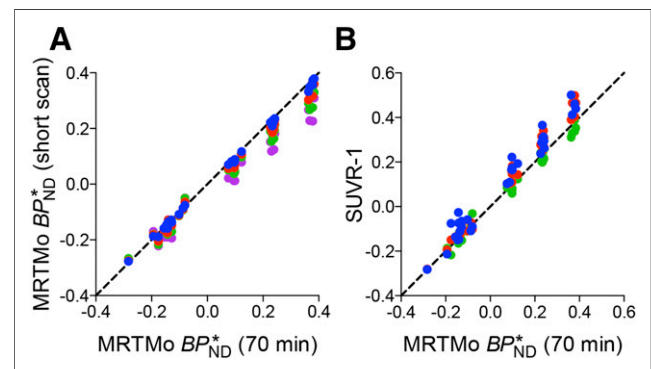


FIGURE 6. Correlation of BP_{ND}^* estimated by MRTM_O and SUVR-1 with scan data of various lengths. (A) BP_{ND}^* values estimated by MRTM_O with 60- (blue), 50- (red), 40- (green), and 30-min (purple) data were plotted against those with full 70-min data. (B) SUVR-1 values with 50- to 70- (blue), 30- to 50- (red), and 20- to 30-min (green) data were plotted against BP_{ND}^* values estimated by MRTM_O with 70-min data.

degree of the ^{11}C -PBB3 metabolisms, and therefore BP_{ND}^* may require a larger effect size for group comparisons. On the other hand, BP_{P} should not suffer from this intersubject variation, but due to its quick metabolism, regular metabolite analysis of ^{11}C -PBB3 is not practical for the estimation of BP_{P} .

We selected SUVR-1 at 30–50 min when specific-binding time–activity curves become relatively flat (Supplemental Fig. 8). SUVR-1 can be practically obtained by a static PET scan initiated at a fixed time point after ^{11}C -PBB3 injections. By contrast, the reference tissue BP_{ND}^* estimation requires dynamic PET data, but the advantage of the reference tissue BP_{ND}^* estimation is its independence of cerebral blood flow or the systemic clearance of the radioligand. BP_{ND}^* therefore should be more suited for long-term longitudinal studies (36).

CONCLUSION

We have established methods for quantification of tau pathology in the human brain using ^{11}C -PBB3. The BP_{ND}^* determined by dual-input graphical analysis models is consistent with the reference tissue BP_{ND}^* and SUVR-1, suggesting that these parameters can accurately quantify target tau deposits notwithstanding the entry of radiometabolites into the brain. MRTM_0 is suitable quantification for ^{11}C -PBB3 without blood data when a patient can be stably scanned for 60 min. If the motion of the patient hampers the dynamic data, SUVR-1 30–50 min can be used as an alternative method. ^{11}C -PBB3 thus appears an adequate radioligand for PET imaging of tau pathology.

APPENDIX

Current BP_{ND}^* from the dual-input graphical analysis and the reference tissue model MRTM_0 with the additional metabolite distribution volume term ($\delta V_{\text{ND}}^{\text{M}}$) can be shown to be directly proportional to $B_{\text{avail}}/K_{\text{D}}$. At equilibrium, $f_{\text{ND}}^{\text{P}} \times C_{\text{ref}}^{\text{P}} = f_{\text{P}}^{\text{P}} \times C_{\text{P}}^{\text{P}}$, thus $V_{\text{ND}}^{\text{P}} = \frac{C_{\text{ref}}^{\text{P}}}{C_{\text{P}}^{\text{P}}} = \frac{f_{\text{P}}^{\text{P}}}{f_{\text{ND}}^{\text{P}}}$, and $f_{\text{ND}}^{\text{M}} \times C_{\text{ref}}^{\text{M}} = f_{\text{P}}^{\text{M}} \times C_{\text{P}}^{\text{M}}$, thus $V_{\text{ND}}^{\text{M}} = \frac{C_{\text{ref}}^{\text{M}}}{C_{\text{P}}^{\text{M}}} = \frac{f_{\text{P}}^{\text{M}}}{f_{\text{ND}}^{\text{M}}}$, then $BP_{\text{ND}}^* = \frac{V_{\text{S}}}{V_{\text{ND}}^{\text{P}} + \delta V_{\text{ND}}^{\text{M}}} = \frac{V_{\text{S}}}{\frac{f_{\text{P}}^{\text{P}}}{f_{\text{ND}}^{\text{P}}} + \delta \frac{f_{\text{P}}^{\text{M}}}{f_{\text{ND}}^{\text{M}}}} = \frac{f_{\text{P}}^{\text{P}} B_{\text{avail}}}{f_{\text{ND}}^{\text{P}} + \delta \frac{f_{\text{P}}^{\text{M}}}{f_{\text{ND}}^{\text{M}}}} \propto \frac{B_{\text{avail}}}{K_{\text{D}}}$, where f_{P}^{P} and f_{P}^{M} are plasma-free fraction for parent and metabolite; f_{ND}^{P} and f_{ND}^{M} , tissue-free fraction for parent and metabolite; C_{P}^{P} and C_{P}^{M} , plasma concentration of parent and metabolite at equilibrium; and $C_{\text{ref}}^{\text{P}}$ and $C_{\text{ref}}^{\text{M}}$, concentration in the reference tissue of parent and metabolite at equilibrium. Because free fractions and δ are all constants, BP_{ND}^* is directly proportional to the binding density, $B_{\text{avail}}/K_{\text{D}}$.

DISCLOSURE

The costs of publication of this article were defrayed in part by the payment of page charges. Therefore, and solely to indicate this fact, this article is hereby marked “advertisement” in accordance with 18 USC section 1734. This study was supported in part by J-AMP of MEXT, Japan; grants-in-aid for scientific research on innovative areas (“Brain Environment”) 23111009 and on young scientists (A) 26713031 from MEXT, Japan; Health Labour Sciences Research grant H25-Seishin-Jituyouka(Seishin)-Ippan-001 from MHLW, Japan; and the Brain Mapping by Integrated Neurotechnologies for Disease Studies from AMED, Japan. No other potential conflict of interest relevant to this article was reported.

ACKNOWLEDGMENTS

We thank Katsuyuki Tanimoto and Takahiro Shiraishi and the members of the Clinical Neuroimaging Team for their support in PET scans, Kazuko Suzuki and Izumi Izumida for their assistance as clinical coordinators, and the staff of the Molecular Probe Program for the radioligand synthesis and metabolite analysis.

REFERENCES

- Braak H, Braak E. Neuropathological staging of Alzheimer-related changes. *Acta Neuropathol (Berl)*. 1991;82:239–259.
- Hardy JA, Higgins GA. Alzheimer’s disease: the amyloid cascade hypothesis. *Science*. 1992;256:184–185.
- Klunk WE, Engler H, Nordberg A, et al. Imaging brain amyloid in Alzheimer’s disease with Pittsburgh Compound-B. *Ann Neurol*. 2004;55:306–319.
- Villemagne VL, Burnham S, Bourgeat P, et al. Amyloid β deposition, neurodegeneration, and cognitive decline in sporadic Alzheimer’s disease: a prospective cohort study. *Lancet Neurol*. 2013;12:357–367.
- Vandenberghe R, van Laere K, Ivanoiu A, et al. ^{18}F -flutemetamol amyloid imaging in Alzheimer disease and mild cognitive impairment: a phase 2 trial. *Ann Neurol*. 2010;68:319–329.
- Jack CR, Knopman DS, Jagust WJ, et al. Tracking pathophysiological processes in Alzheimer’s disease: an updated hypothetical model of dynamic biomarkers. *Lancet Neurol*. 2013;12:207–216.
- Arriagada PV, Growdon JH, Hedley-Whyte ET, Hyman BT. Neurofibrillary tangles but not senile plaques parallel duration and severity of Alzheimer’s disease. *Neurology*. 1992;42:631–639.
- Roberson ED, Scearce-Levie K, Palop JJ, et al. Reducing endogenous tau ameliorates amyloid β -induced deficits in an Alzheimer’s disease mouse model. *Science*. 2007;316:750–754.
- Giacobini E, Gold G. Alzheimer disease therapy: moving from amyloid- β to tau. *Nat Rev Neurol*. 2013;9:677–686.
- Zhang B, Maiti A, Shively S, et al. Microtubule-binding drugs offset tau sequestration by stabilizing microtubules and reversing fast axonal transport deficits in a tauopathy model. *Proc Natl Acad Sci USA*. 2005;102:227–231.
- Dickson DW. Neuropathologic differentiation of progressive supranuclear palsy and corticobasal degeneration. *J Neurol*. 1999;246(suppl 2):II6–II15.
- Dickson DW. Neuropathology of Pick’s disease. *Neurology*. 2001;56:S16–S20.
- Jack CR, Knopman DS, Jagust WJ, et al. Hypothetical model of dynamic biomarkers of the Alzheimer’s pathological cascade. *Lancet Neurol*. 2010;9:119–128.
- Wischik C, Staff R. Challenges in the conduct of disease-modifying trials in AD: practical experience from a phase 2 trial of TAU-aggregation inhibitor therapy. *J Nutr Health Aging*. 2009;13:367–369.
- Maruyama M, Shimada H, Suhara T, et al. Imaging of tau pathology in a tauopathy mouse model and in Alzheimer patients compared to normal controls. *Neuron*. 2013;79:1094–1108.
- Villemagne VL, Furumoto S, Fodero-Tavoletti MT, et al. In vivo evaluation of a novel tau imaging tracer for Alzheimer’s disease. *Eur J Nucl Med Mol Imaging*. 2014;41:816–826.
- Okamura N, Furumoto S, Fodero-Tavoletti MT, et al. Non-invasive assessment of Alzheimer’s disease neurofibrillary pathology using ^{18}F -THK5105 PET. *Brain*. 2014;137:1762–1771.
- Villemagne V, Rowe C, Tamagnan G, et al. In vivo tau imaging with ^{18}F -THK5105 and ^{18}F -THK5117. *Alzheimers Dement*. 2014;10(suppl):P241.
- Okamura N, Furumoto S, Harada R. Characterization of [^{18}F] THK-5351, a novel PET tracer for imaging tau pathology in Alzheimer’s disease [abstract]. *Eur J Nucl Med Mol Imaging*. 2014;41(suppl 2):S260.
- Xia C-F, Arteaga J, Chen G, et al. [^{18}F]T807, a novel tau positron emission tomography imaging agent for Alzheimer’s disease. *Alzheimers Dement*. 2013;9:666–676.
- Chien DT, Szardenings AK, Bahri S, et al. Early clinical PET imaging results with the novel PHF-tau radioligand [F18]-T808. *J Alzheimers Dis*. 2014;38:171–184.
- Shimada H, Higuchi M, Shinotoh H, et al. In vivo visualization of tau pathology in Alzheimer’s disease patients by [^{11}C]PBB3-PET. *Alzheimers Dement*. 2013;9(suppl):P845.
- Hashimoto H, Kawamura K, Igarashi N, et al. Radiosynthesis, photoisomerization, biodistribution, and metabolite analysis of ^{11}C -PBB3 as a clinically

- useful PET probe for imaging of tau pathology. *J Nucl Med.* 2014;55:1532–1538.
24. Ichise M, Fujita M, Seibyl JP, et al. Graphical analysis and simplified quantification of striatal and extrastriatal dopamine D₂ receptor binding with [¹²³I] epidepride SPECT. *J Nucl Med.* 1999;40:1902–1912.
 25. Fujita M, Seibyl JP, Verhoeff NP, et al. Kinetic and equilibrium analyses of [¹²³I] epidepride binding to striatal and extrastriatal dopamine D₂ receptors. *Synapse.* 1999;34:290–304.
 26. McKhann G, Drachman D, Folstein M, Katzman R, Price D, Stadlan EM. Clinical diagnosis of Alzheimer's disease: report of the NINCDS-ADRDA Work Group under the auspices of Department of Health and Human Services Task Force on Alzheimer's Disease. *Neurology.* 1984;34:939–944.
 27. Morris JC. The Clinical Dementia Rating (CDR): current version and scoring rules. *Neurology.* 1993;43:2412–2414.
 28. Folstein MF, Folstein SE, McHugh PR. "Mini-mental state": a practical method for grading the cognitive state of patients for the clinician. *J Psychiatr Res.* 1975;12:189–198.
 29. Innis RB, Cunningham VJ, Delforge J, et al. Consensus nomenclature for in vivo imaging of reversibly binding radioligands. *J Cereb Blood Flow Metab.* 2007;27:1533–1539.
 30. Varrone A, Tóth M, Steiger C, et al. Kinetic analysis and quantification of the dopamine transporter in the nonhuman primate brain with ¹¹C-PE2I and ¹⁸F-FE-PE2I. *J Nucl Med.* 2011;52:132–139.
 31. Logan J, Fowler JS, Volkow ND, Wang GJ, Ding YS, Alexoff DL. Distribution volume ratios without blood sampling from graphical analysis of PET data. *J Cereb Blood Flow Metab.* 1996;16:834–840.
 32. Mintun MA, Raichle ME, Kilbourn MR, Wooten GF, Welch MJ. A quantitative model for the in vivo assessment of drug binding sites with positron emission tomography. *Ann Neurol.* 1984;15:217–227.
 33. Ichise M, Liow J-S, Lu J-Q, et al. Linearized reference tissue parametric imaging methods: application to [¹¹C]DASB positron emission tomography studies of the serotonin transporter in human brain. *J Cereb Blood Flow Metab.* 2003;23:1096–1112.
 34. Herrmann M, Golombowski S, Kräuchi K, et al. ELISA-quantitation of phosphorylated tau protein in the Alzheimer's disease brain. *Eur Neurol.* 1999;42:205–210.
 35. Ichise M, Cohen RM, Carson RE. Noninvasive estimation of normalized distribution volume: application to the muscarinic-2 ligand [¹⁸F]FP-TZTP. *J Cereb Blood Flow Metab.* 2008;28:420–430.
 36. van Berckel BNM, Ossenkoppele R, Tolboom N, et al. Longitudinal amyloid imaging using ¹¹C-PiB: methodologic considerations. *J Nucl Med.* 2013;54:1570–1576.